**University of Plymouth**

**PEARL** **https://pearl.plymouth.ac.uk**

01 University of Plymouth Research Outputs University of Plymouth Research Outputs

2016-12

# CFD investigations of OXYFLUX device, an innovative wave pump technology for artificial downwelling of surface water

Antonini, A

http://hdl.handle.net/10026.1/8679

10.1016/j.apor.2016.10.002
Applied Ocean Research

*All content in PEARL is protected by copyright law. Author manuscripts are made available in accordance with publisher policies. Please cite only the published version using the details provided on the item record or document. In the absence of an open licence (e.g. Creative Commons), permissions for further reuse of content should be sought from the publisher or author.*

# CFD INVESTIGATIONS OF OXYFLUX DEVICE, AN INNOVATIVE WAVE PUMP TECHNOLOGY FOR ARTIFICIAL DOWNWELLING OF SURFACE WATER

Alessandro Antonini[a]*, Alberto Lamberti[b], Renata Archetti[b] and Adrià Moreno Miquel[b]

**[a] School of Marine Science and Engineering, University of Plymouth, Marine Building, Drake Circus, Plymouth, Devon, PL4 8AA**

**[b] DICAM, University of Bologna, Via Risorgimento 2, Bologna, 40136, Italy**

*** Corresponding author: School of Marine Science and Engineering, University of Plymouth, Marine Building, Drake Circus, Plymouth, Devon, PL4 8AA.**
**Email address: alessandro.antonini@plymouth.ac.uk;**

**Keywords:** OXYFLUX; Anoxia; CFD; Overset grid; Wave Energy; Floating body

## Abstract

No other environmental variable of such ecological importance to estuarine and coastal marine ecosystems around the world has changed so drastically, in such a short period of time, as dissolved oxygen in coastal waters. The prevalent methods for counteracting anoxic sea events are indirect measures which aim to cut-down anthropic loads introduced in river and marine environments. To date, no direct approaches, like artificial devices have been investigated except the WEBAP and OXYFLUX devices. The present paper adopts a numerical approach to the analysis of the pumped surface water as well as the analysis of the dynamic response of the OXYFLUX device. By means of a CFD-RANS code and through the application of overset grid method, the 1/16 OXYFLUX model's dynamic response and pumping performance are evaluated. The appropriate grid is selected after an extensive sensitivity analysis carried out on 9 different grids. The CFD model is validated by comparing numerical and physical results of heave decay test, heave response, and surface water discharge under the action of regular waves. The extensive comparison with experimental results shows consistently accurate predictions. The main findings of the study show that nonlinear effects remarkable reduce the dynamic behaviour of the OXYFLUX and generate an unexpected second harmonic for pitch response intensifying the overtopping discharge also for small waves caused by the summer's low intensity winds.

## 1. Introduction

Several areas in the world are affected by hypoxia (the condition of low concentrations of dissolved oxygen) following the eutrophication, which results from nutrient problem. The primary factor driving coastal eutrophication is an imbalance in the nitrogen cycle that can be directly linked to high anthropic pressure

mainly due to the urbanization in coastal areas or along rivers. One of the recent investigation on the hypoxic worldwide zones linked them with the very densely populated coastal area that deliver large quantities of nutrients, [1]. Two principal factors lead to the development of hypoxia: i) the decrease of water exchange between bottom water and oxygen-rich surface water and ii) decomposition of organic matter in the bottom water, which reduces oxygen levels. Both conditions are necessary for the development and persistence of hypoxia, [2-3].

Within the past 50 years, different concepts and ideas of devices have been proposed to pump water vertically in the ocean. Their aims were to pump nutrient rich water from the ocean bottom to the surface, where nutrients can be used to increase the fishery production, [4–8]. More recently, a new type of device aimed to pump water downward through the water column, by means of the wave energy captured through the overtopping, have been analyzed. Two major purposes lead such new technologies; the first is the extraction of clean energy from wave motion [9], and the second, which is also the purpose of the OXYFLUX device, is to pump well oxygenated surface water to the bottom, where oxygen is required [10–12].

To convert wave energy into useful power, a wide variety of Wave Energy Converter (WEC) designs have been proposed, including oscillating water columns, bottom-hinged pitching devices, floating pitching devices, overtopping devices, and point absorbers. The overtopping converters have advantages that distinguish them from other devices. First of all, the fluctuations of the energy produced by these devices are, in fact, relatively small, since the conversion takes place in calm conditions at the reservoir where water is temporarily stored. Furthermore, the use of a ramp, which focuses the entry of water into the basin, makes possible the use of such a device even in non-favorable coastal regions characterized by a low density of wave energy. Finally, they can be realized as circular shaped devices without any requirements on the main wave direction.

The proposed OXYFLUX device is the same that was previously experimentally analysed by Antonini et al. 2015, [10;39]. It consists of an hybrid between a point absorber and an overtopping device. Since its dynamic behaviour is governed by the same principles of a point absorber while at the same time takes advantage of the wave which overtops the floater surface.

Generally, the dynamic response of the point absorber system and its power extraction performance can be obtained by solving the equation of motion in frequency, [12,13] or in time domain, [14]. In particular, time domain approach has been often used in the study of optimal control and tuning strategies for point absorbers [15,16]. To model the floating overtopping devices more complicated methods are needed. The overtopping phenomenon is characterized by strong non-linearities requiring non-linear numerical models or a physical approach, [17]. Therefore, to predict the pumping performance more accurately, a

comprehensive study of the OXYFLUX device that considers nonlinear interactions by using Computational Fluid Dynamics (CFD) methods are needed. CFD methods have been widely used to model the complex nonlinear hydrodynamics generated by wave and floating body interaction, including the analyses of several types of WEC systems, [18–21]. Moreover, the overtopping phenomenon can be barely modelled through empirical formulas, which in turn, does not fit all kinds of devices due to their experimental nature. The hydrodynamics of the OXYFLUX is particularly complex. In fact, the problem involves the interaction between waves and the whole body, including the floating part, the submerged part and the overtopping ramp on the floater. In this paper, by means of CFD overset grid method, [22], the numerical analysis of the OXYFLUX, is proposed. Specifically, this study aims to: *i)* validate the developed numerical model in order to define a reliable tool for the optimization phase, *ii)* investigate nonlinear effects of the interaction between waves and the OXYFLUX on its pumping performance and its dynamic response.

The paper is composed of the following: in *section 2*, OXYFLUX 1/16 Froude scale geometry is described. In *section* 3, the theoretical device background is proposed while in *section* 4, a brief description of the experimental facility is presented in order to let the reader get the basic concepts of the adopted methodology useful to understand those physical results used in this work. In *section* 5, the computational methodology is described. In *section 6*, the grid sensitivity analysis and validation study are discussed. In *section 7*, the results are shown and interpreted. And finally, in *section 8,* the conclusions are drafted.

## 2. OXYFLUX geometry and dimension

In this paper the analysed device is fully based on the shape, geometry and mass distribution adopted in the physical study carried out by Antonini et al. 2015, [10]. OXYFLUX is composed by three main parts: *i*) truncated-conical floater, *ii*) connecting pipe and *iii*) stabilizing ring; 1/16 Froude scale model is presented in Figure 1. Buoyancy of the whole structure is entrusted to a truncated-conical floater, which as well as keeping the structure afloat also collects the water from overtopping. The connection with the bottom, (where a stabilizing ring is mounted), is fastened by means of a rigid pipe. The final design of the scaled OXYFLUX consists of a truncated conical shape with a volume of 227’191 $mm^3$, with a weight of 0.11 N. Its maximum diameter is equal to 150 mm while its height is 30 mm. The pipe connects the floater,(where the water is stored), to the bottom, (where the water flows out from the device). The weight of the tube is 1.15 N, the internal diameter has been kept equal to 50 mm where a rigid structure aimed to support the Doppler transducer (hereinafter referred to as DOP) is mounted.

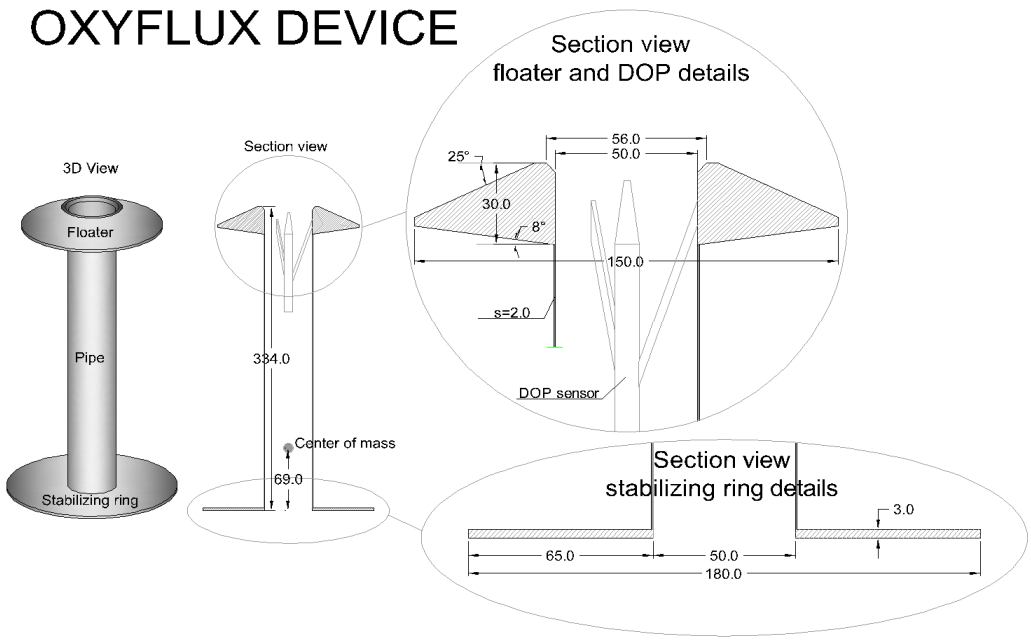


Figure 1: Details of the OXYFLUX model, all lengths are in mm.

The function of the stabilizing ring is to dampen the heave motion in order to let the wave crest to overtop the floater. The ring is 3 mm thick, its diameter is 180 mm and its weight is 1.88 N. The total length of the device model is 334 mm, from the lower surface of the stabilizing ring to the top of the floater ( see Figure 1). The water level stays seven millimeters under the floater top; the position of the center of gravity is largely affected by the difference in density of the components, and it is located 265 mm below the water level when the device is at rest. The position of the center of gravity largely below the center of buoyancy, was chosen in order to improve the stability of the device under the waves action. The total weight of the model is 3.17 N while the maximum buoyancy force is 3.39 N ensuring a buoyancy reserve force of 0.22 N, which is 6.5 % of the total weight. More than 60 % of its weight is concentrated along the first 8 mm of the device, which means that the weight of the stabilizing ring leads to a really deep center of mass ensuring the required reserve of stability, Figure 2. The gyration radius, with respect to the center of mass, are: $R_{xx}=R_{yy}=223$ mm and $R_{zz}=50$ mm.

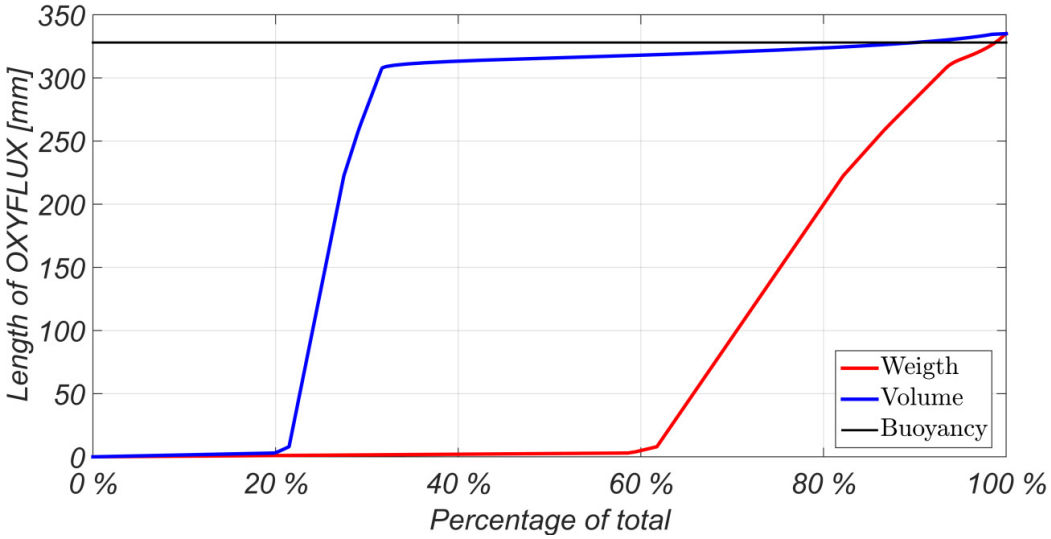


Figure 2: Volume and weight distribution of the OXYFLUX model. On the y-axis the length of the model is shown (origin is posed at the lower surface of the stabilizing ring), while on the x-axis the percentage related to the total model volume and weight is plotted.

## 3. OXYFLUX: the proof of concept

OXYFLUX, has been designed for typical conditions causing anoxia, in particular for an operating range of incident wave heights characteristic of the summer climate, (i.e. small wave heights due to the breeze). The design have been performed taking into consideration the climate and physical conditions typical of the Northern Adriatic Sea; as this is a site suffering from severe summer anoxia. The typical Northern Adriatic summer vertical density profiles, Figure 3, are derived from Artegiani et al. (1997), [23], while the wave climate is derived from the analysis of waves data collected by the wave buoy Nausicaa, [24, 25].

The physical principle of the device is rather simple. It is based on its capacity to enhance vertical mixing processes and to induce aeration of deep water by pumping oxygen-rich surface water downward at a desired depth around the halocline driven by the action of small waves. Its operating mechanism is based on flux caused by the wave overtopping. The floater collects incoming waves into a reservoir floating on the sea. Water overtopping yields a higher hydraulic head in the reservoir, which in turn induces a downward water flux.

Water flux generated by the OXYFLUX needs a sufficient head to induce the water column motion. The evaluation of this quantity is made on the basis of basic hydraulic calculation: the minimum head must overcome the following components: head losses in the pipe (plus inlet and outlet losses) and losses related to the different water density along the vertical water column. Furthermore, a depth of 6.4 m has been considered during the design phase, according to the field conditions for the Northern Adriatic, where it is common for symptoms of eutrophication and hypoxia to arise between 5 and 10 m of water depth.

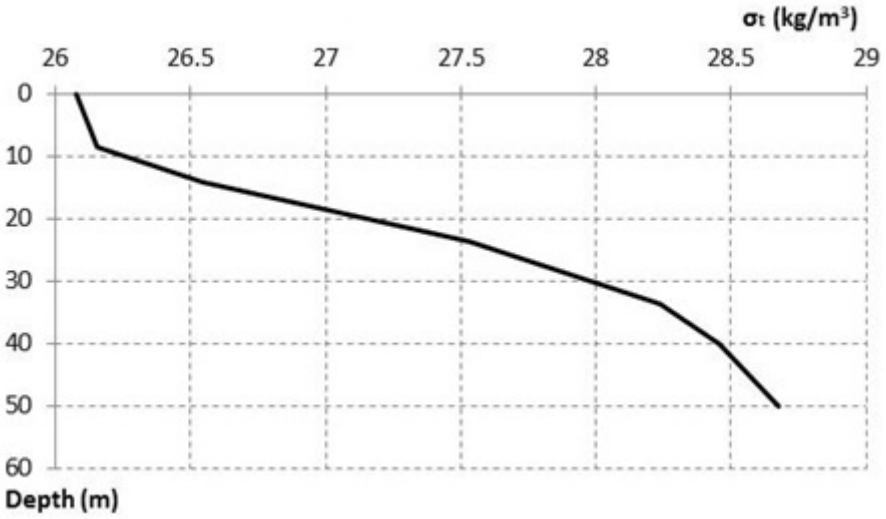


Figure 3 Summer density anomaly in North Adriatic, (Artegiani et al., 1997).

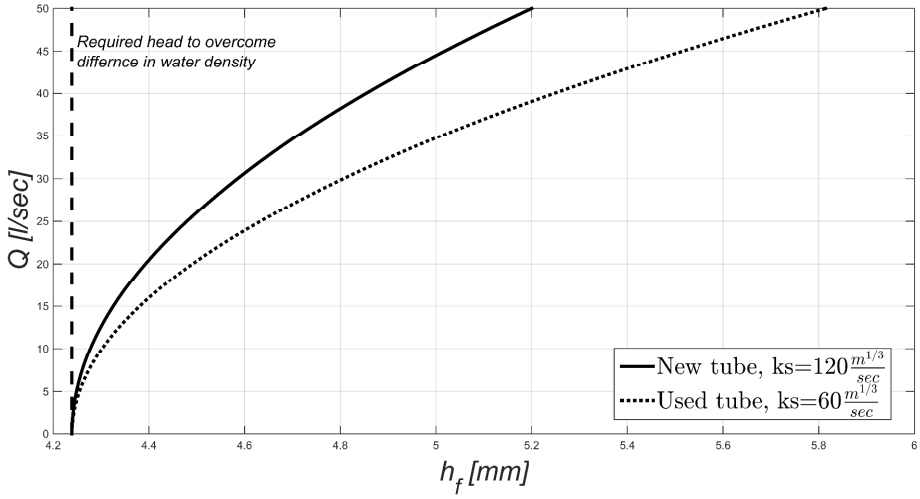


Figure 4: Device capacity for 10 m depth for different heads and material conditions. Pipe characteristics: 5.36 m long 0.80 m diameter.

The minimum head to overcome the density difference ($\Delta h_\rho$) has been calculated by means of the application of Kelvin's circulation theorem considering field condition, i.e. 6.4 m water depth and a real density profile. The application of Kelvin's theorem implies that the water column inside the device has been considered to be made up of only lighter surface water pushed downward by the requested minimum head. This phenomenon has been modeled as a circular integral on a closed path from the surface to the desired depth in which one vertical branch of the path is characterized by a surface density and the other by the density profile proposed in Figure 3. Eq (1) summarizes the described model:

$$\Delta h_\rho = \frac{\sum_1^n(\rho_i \cdot l_i) - \rho_1 \cdot L}{\rho_1} \qquad (1)$$

where $\rho_i$ is the density of the "$i$" layer, $l_i$ is the thickness of the "$i$" layer equal to 0.01 m , $\rho_1$ is the water density at the surface equal to 1026.10 kg/m$^3$ and $L$ is the desired depth to reach. Distributed and concentrated pressure drops have been calculated by means of the classical Chezy formula.

Figure 4 presents the estimated flow rate ($Q$) as function of required head ($h_f$). For 5.36 m long pipe with 0.8 m diameter, the pipe capacity has been calculated for different heads and 2 roughnesses associated with different materials conditions of the pipe. The resulting minimum head needed to overcome the water density difference is slightly larger than 4 mm, while the distributed and concentrated pressure drops increase with the increasing of the channeled water flow.

Despite the design phase has considered prototype dimension and field application with a real stratification, in this study we present the results of a numerical simulations carried out with a depth of 0.4 m, same value adopted in the 1:16 Froude scale physical modelling proposed by Antonini et al. 2015, [10;39]. Moreover, considering the negligible order of magnitude of the required head to overcome the water density difference the following numerical simulation do not take into account the stratification effect.

## 4. Experimental wave flume tests

The experimental tests are carried out in the wave flume at the Hydraulic Laboratory of the University of Bologna (LIDR, http://www.dicam.unibo.it/Centro-laboratori/lidr) in order to verify the presumed proof of concept assumed during the design phase and to validate the numerical prediction. The wave flume is 12.50 m long (9.75 m available considering wave maker and wave absorber), 0.50 m wide with a maximum depth of 0.70 m. Figure 5 shows the wave tank dimension, the experimental settings and the 1:16 OXYFLUX physical model. A more detailed description of the physical modelling and of the flume setup are discussed in [10]. A 2D motion tracking system is used to capture the OXYFLUX's motion. The motions are captured as a 2D projection, orthogonal to the direction of wave propagation in the flume. The incident wave is measured by means of 3 wave gauges installed in front of the device along the flume axis. The model is anchored by four pre-tensioned nylon cables, which allow the heave displacements and damping the horizontal ones, (surge). A Doppler velocimetry system (DOP2000 by Signal Processing S.A.) measures the water velocity inside the device: a single probe connected to an ultrasonic doppler velocity profiler is installed along the pipe axis of the physical model at a distance equal to 40 mm from the top of the floater. The active part of the transducer has a diameter of 5.00 mm and is housed in a 8.00 mm diameter plastic cylinder with length equal to 90.00 mm. The connection between the probe and the OXYFLUX model is guaranteed by means of a rigid structure composed by 3 thin arms glued to the transducer case and to the internal surface of the floater, as sketched in Figure 1. Both DOP probe and its support are considered for numerical simulations.

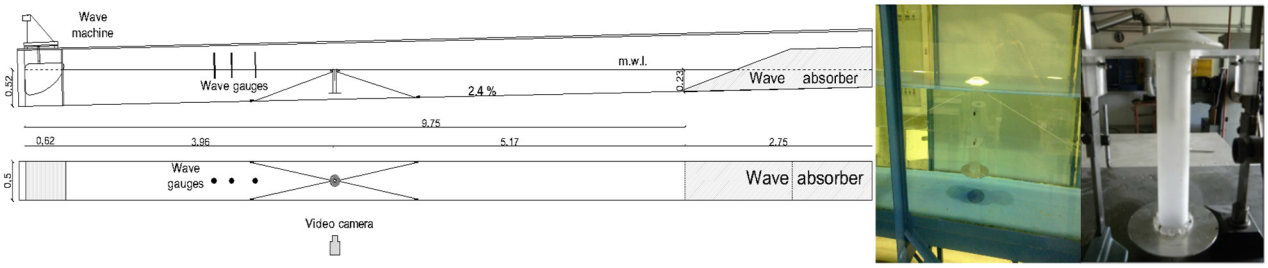


Figure 5 Experimental wave flume and OXYFLUX physical model

## 5. Numerical modelling setup

### *4.1 Mathematical formulation of RANS method*

In this study an Unsteady Reynolds-Averaged Navier–Stokes (URANS) method has been used to solve the governing equations by means of CFD software STAR-CCM+, [26]. The Navier-Stokes equations for incompressible flows are discretized over a computational overset mesh using a finite volume method; their integral form can be written as:

$$\begin{aligned} &\frac{\partial}{\partial t}\int_V \rho \cdot dV + \oint_A \rho \cdot (\boldsymbol{v} - \boldsymbol{v_g}) \cdot da = 0 \\ &\frac{\partial}{\partial t}\int_V \rho \cdot \boldsymbol{v} \cdot dV + \oint_A \rho \cdot \boldsymbol{v} \otimes (\boldsymbol{v} - \boldsymbol{v_g}) \cdot d\boldsymbol{a} = \oint_A (\boldsymbol{T} - p\boldsymbol{I}) \cdot d\boldsymbol{a} + \int_V \boldsymbol{f} \cdot dV \end{aligned} \quad (2)$$

Where $\rho$ is the fluid density, $V$ is the cell volume bounded by the closed surface $A$, $\boldsymbol{v}$ is the velocity vector, $\boldsymbol{v_g}$ is the grid velocity vector, $t$ is the time, $\boldsymbol{T}$ is the viscous stress tensor, and $\boldsymbol{f}$ is the body force terms vector. Viscous stress tensor for turbulent flow is defined as the sum of the laminar and turbulent stress tensors, and under the Boussinesq approximation is described by:

$$\boldsymbol{T}_l = \mu \cdot \left[\nabla \boldsymbol{v} + \nabla \boldsymbol{v}^T - \frac{2}{3} \cdot (\nabla \cdot \boldsymbol{v})\boldsymbol{I}\right] \quad (3)$$

$$\boldsymbol{T}_t = 2 \cdot \mu_t \cdot \boldsymbol{S} - \frac{2}{3} \cdot (\mu_t \nabla \cdot \boldsymbol{v} + \rho \cdot k)\boldsymbol{I} \quad (4)$$

$$\boldsymbol{S} = \frac{1}{2} \cdot (\nabla \boldsymbol{v} + \nabla \boldsymbol{v}^T) \quad (5)$$

$$\boldsymbol{T} = \boldsymbol{T}_t + \boldsymbol{T}_l \quad (6)$$

Where $\mu$ is the laminar viscosity, $\mu_t$ is the turbulent viscosity, $k$ is the turbulent kinetic energy and $\boldsymbol{S}$ is the strain tensor. In this study a k–ω SST turbulence model [27] is applied with a two-layer all y+ wall treatment model, and a second order implicit scheme was utilized for time marching. The transient SIMPLE algorithm is applied to linearize the equations and to achieve pressure–velocity coupling. A volume of fluid method (VOF) is applied to describe the free surface, and an overset mesh model is adopted to follow the body movements and adjust the grids around the OXYFLUX. The resulting system of algebraic equations is then solved using an algebraic multi-grid method. The coupled system of equations is solved in a segregated manner, which means that while the system is solved for each variable, other variables are treated as

known. Note that the equation of motion is coupled with the flow field simulation through iterations. The dynamic response of the floating body is calculated by integrating the acceleration obtained from the equation of motion solution using an implicit algorithm. The body is then moved to a new position and the grid attached to the moving boundaries is updated. The convergence of the coupling between the RANS simulation and the dynamics of the body is reached at each time step.

### *4.2 VOF method*

The VOF method, introduced by [28], is an interface capturing method without reconstruction and hence, does not treat the free surface as a sharp boundary. The calculation is performed on a grid and free surface interface orientation and shape are calculated as a function of the volume fraction of the respective fluid within a control volume. The VOF method employs the concept of an equivalent fluid. This approach assumes that the fluid phases share the same velocity and pressure fields; the momentum and mass transport equations are solved as in a single-phase flow condition. The volume fraction $\alpha_i$ describes to which level the cell is filled with the respective fluid. Free surface is then defined as the isosurface at which the volume fractions take the value of 0.5. The physical properties of the equivalent fluid within a controlled volume are calculated as functions of the physical properties of the phases and their volume fractions. The critical issue for this kind of method is the discretization of the convective term, which required higher order schemes. The simulations presented in this paper are carried out according the HRIC (High Resolution Interface Capturing) scheme which is a convective scheme based on the normalized variable diagram, [29].

### *4.3 Dynamic overset grid approach*

The main motivations behind the overset grid originated from the requirement to perform simulations involving multiple bodies in large relative motion, [22,30]. Rigid and deforming mesh motion, available in STAR-CCM+ show several disadvantages compared to the overset mesh approach, when simulating bodies with large amplitude motions. Rigid motion approach causes difficulties for free surface refinement, especially in pitch [31]. And deforming meshes may lead to cell quality problems, [30]. This approach implies a domain discretized by a static grid (*background region*) and a moving grid (*overset region*). The static grid is fixed to the earth system and therefore does not move. This grid is designed to properly resolve the air-water interface and the incident waves, and extends far enough from the OXYFLUX device so that the far-field boundary conditions are imposed only on static grids. The background region encloses the entire solution domain and the smaller region containing the device body. The moving, rigid region is attached to the OXYFLUX and it will move according to the predicted translation motions described with eq. (6). In an overset mesh, cells are grouped in; active, inactive or as acceptor cells. Within active cells, discretized governing equations are solved. Within inactive cells, no equation is solved. However, these

cells can become active if the overset region is moving. Lastly, there are acceptor cells, which separate active and inactive cells in the background region and are attached to the overset boundary in the overset region. The solution is computed for all active cells in all regions simultaneously, that is, the meshes are implicitly coupled. The use of the overset mesh saves computational costs, and allows the generation of a sufficiently refined mesh configuration around the free surface and the body without compromising the solution's accuracy.

### *4.4 Response calculation*

Through Newton's Law, OXYFLUX movements, accelerations and velocities are calculated under the simplification of two degrees of freedom (i.e. heave and pitch), rigid body and absence of the mooring system. The OXYFLUX device predominantly operates in heave, but at the same time it takes advantage from the wave which overtops its floater consequently the realistic simulation of the pumping performance requires the pitch to be thoroughly modelled. The equations of motion for OXYFLUX's heave and pitch modes, according to [32], are the following:

$$m \cdot \frac{d\boldsymbol{v_c}}{dt} = \boldsymbol{F}$$
$$\boldsymbol{I} \cdot \frac{d\boldsymbol{\omega_c}}{dt} = \boldsymbol{M} \qquad (7)$$

where $m$ is the total mass of the rigid body, $\boldsymbol{v_c}$ and $\boldsymbol{\omega_c}$ are linear and angular velocities about the center of mass, $\frac{d}{dt}$ indicates the time derivative, $\boldsymbol{I}$ is the moment of inertia about the center of mass, $\boldsymbol{M}$ and $\boldsymbol{F}$ are the total torque and force on the rigid body. The resultant forces and torque acting on the rigid body are calculated by integrating the fluid pressure on each body surface. The mooring system is neglected in this study according to Muliawan et al., (2013) and Yu and Li, (2011) who highlighted the negligible effect of the mooring system on the energy production of a single and two bodies point absorber WEC, [18,33]. Due to the similarity between the OXYFLUX and these WEC types we assumed that also for the pumping performance of the OXYFLUX device the effects of the mooring lines might be neglected.

## 6. OXYFLUX modelling

### *5.1 Domain and boundary conditions*

The computational domain is divided in two main regions: background and overset region. A right-handed Cartesian coordinate system is located at the OXYFLUX's revolution axis. The longitudinal x-axis is pointing towards the outlet boundary, the z-axis is vertical and points upwards, and the undisturbed free surface is the plane z=0. The origin of the coordinates is located at the intersection of the free surface, the

longitudinal section of the domain (y=0) and the transverse section of the device (x=0). The background region is 0.50 m wide ( -0.25 ≤ *y* ≤ 0.25) according the wav flume used for the physical test, 0.75 m high ( -0.53 ≤ *z* ≤ 0.22 ) and its length varies according to the simulated wavelength ($-\lambda \leq x \leq 3 \cdot \lambda$). Overset region is a squared-section parallelepiped, 0.44 m high ( -0.38 ≤ *z* ≤ 0.06) and 0.25 m wide ( -0.125 ≤ *x*; *y* ≤ 0.125 ). A schematic is presented in Figure 4 and Figure 7. The device's location is placed in order to have its vertical revolution axis passing through x=*y*=0.00. Such a domain configuration ensures a suitable overlapping of the two regions and an adequate gap between background and overset region's boundaries. Furthermore, dimensions of the overset region allow to keep at least four layers of cell between the device surface and the overset boundaries. The seabed is given at 0.40 m below the mean water surface, and a 1st order wave velocity profile is specified at the up-wave boundary, (see Figure 6). The pressure outlet is implemented at the down-wave boundary. VOF wave damping layer is applied in front of the outlet boundary in order to reduce the reflected wave according to[34]. All the simulations are carried out using a damping zone equal to 2 wavelengths as proposed by [18,35], thus ensuring a gap equal to one wavelength between the damped zone and the device's vertical axis, (see Figure 6). The water flow due to the wave overtopping is measured through an artificial interface generated on the top of the floater (see Figure 6).

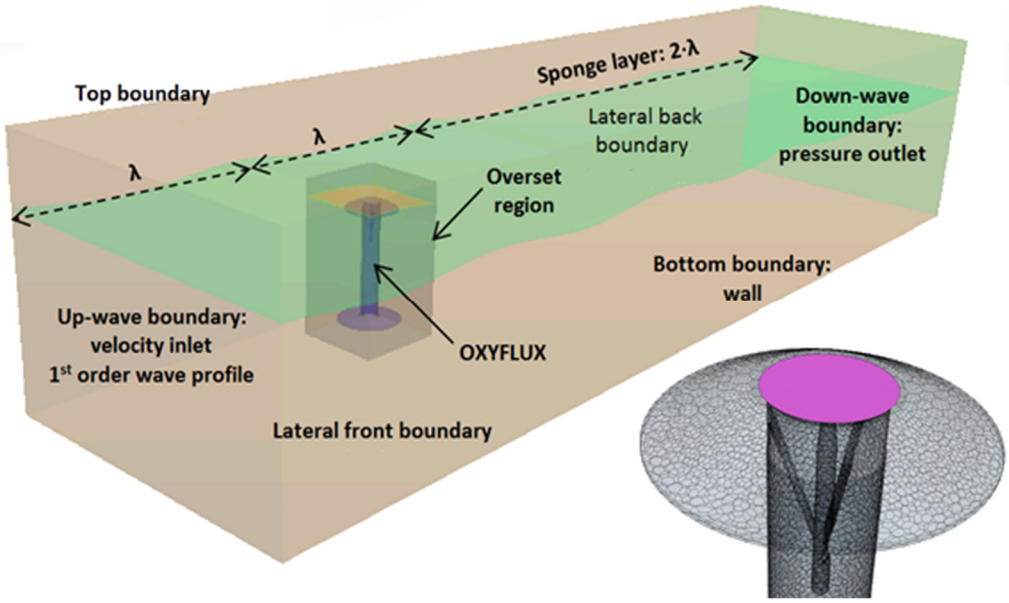


Figure 6 3D numerical domain, regions, used boundaries conditions and adopted artificial interface for measuring water flow

Five boundary conditions have been used to describe the fluid field at the domain bounds. They include: no-slip wall and slip wall, velocity inlet, pressure outlet and overset mesh condition. No-slip wall boundary condition represents an impenetrable, no-slip condition for viscous flow, such boundary is used to describe the device surface. Slip wall boundary condition is applied to describe top (z=0.22 m), bottom (z=-0.53) and lateral boundaries (y=-0.25 and y=0.25 m) of the domain. The use of the slip wall boundary condition at the top, sides and bottom of the background aims to better reproduce the laboratory condition, including reflection of the wave due to the lateral boundary. These are made by means of glass walls in the physical

wave flume. Velocity inlet boundary represents the inlet of the domain at which the flow velocity is known according to the required wave profile. This condition is used to model the up-wave boundary at $x = -\lambda$.

The pressure outlet boundary is a flow outlet boundary for which the pressure is specified, in this model we used condition of calm water surface, outlet boundary is imposed at $x = 3 \cdot \lambda$. The boundary face velocity is extrapolated from the interior of the domain using reconstruction gradients, while boundary pressure can have two different calculation methods. If inflow occurs, pressure is defined by the following equation:

$$p = p_{specified} - \frac{1}{2} \cdot \rho \cdot |\boldsymbol{v}_n|^2 \qquad (8)$$

where $\boldsymbol{v}_n$ is the normal component of the boundary inflow velocity. Whereas, if no inflow occurs the boundary pressure is kept equal to the specified one. The overset region is defined by means of overset mesh boundary, which describes outer boundaries of the region. Such a boundary condition allows the coupling of the overset region with the background region by means of linear interpolation between acceptor and donor cells.

### *5.2 Grid generation and resolution studies*

The overset and prism layer grids are generated using the mesh generator in STAR-CCM+. Grid resolution is finer near the free surface and around the OXYFLUX to capture both the wave dynamics and the details of the flow around the device (see Figure 7). Moreover, a thinner zone containing overset region is created in order to generate an overlapping area with similar cell sizes, background and overset mesh for both. Prism-layer cells are generated along the OXYFLUX surface, the height of the first layer is set so that the value of y+ (10 to 400) satisfies the turbulence model requirement by solving the velocity distribution outside the viscous sub-layer, i.e. buffer layer and log-law regions are solved, [36,37]. Background region is discretized by regular hexahedral cells and three thinner volumes are used to capture the free surface movements and the device dynamics, ($V_{B1}$, $V_{B2}$ e $V_{BO}$). The grid refinements across the water surface are realized by the volumetric controls $V_{B1}$ and $V_{B2}$ proposed along the entire domain, Figure 7. $V_{B2}$'s height is equal to the simulated wave height while $V_{B1}$'s height is 50% more (see longitudinal section in Figure 9). $V_{B2}$*'s* horizontal *g*rid size ($\Delta x = \Delta y$) is determined by the incident wave length $\lambda_i$, while vertical grid size ($\Delta z$) is adjusted according to the incident wave height, $H_i$. The required overlapping area characterized by similar cell size for both background and overset regions is entrusted to the third volumetric control $V_{BO}$ which is defined by a squared parallelepiped discretized by regular hexahedral cells. Irregular polyhedral cells, with characteristic dimension equal to $V_{BO}$'s $\Delta z$, are adopted to discretize the overset region, Figure 7.

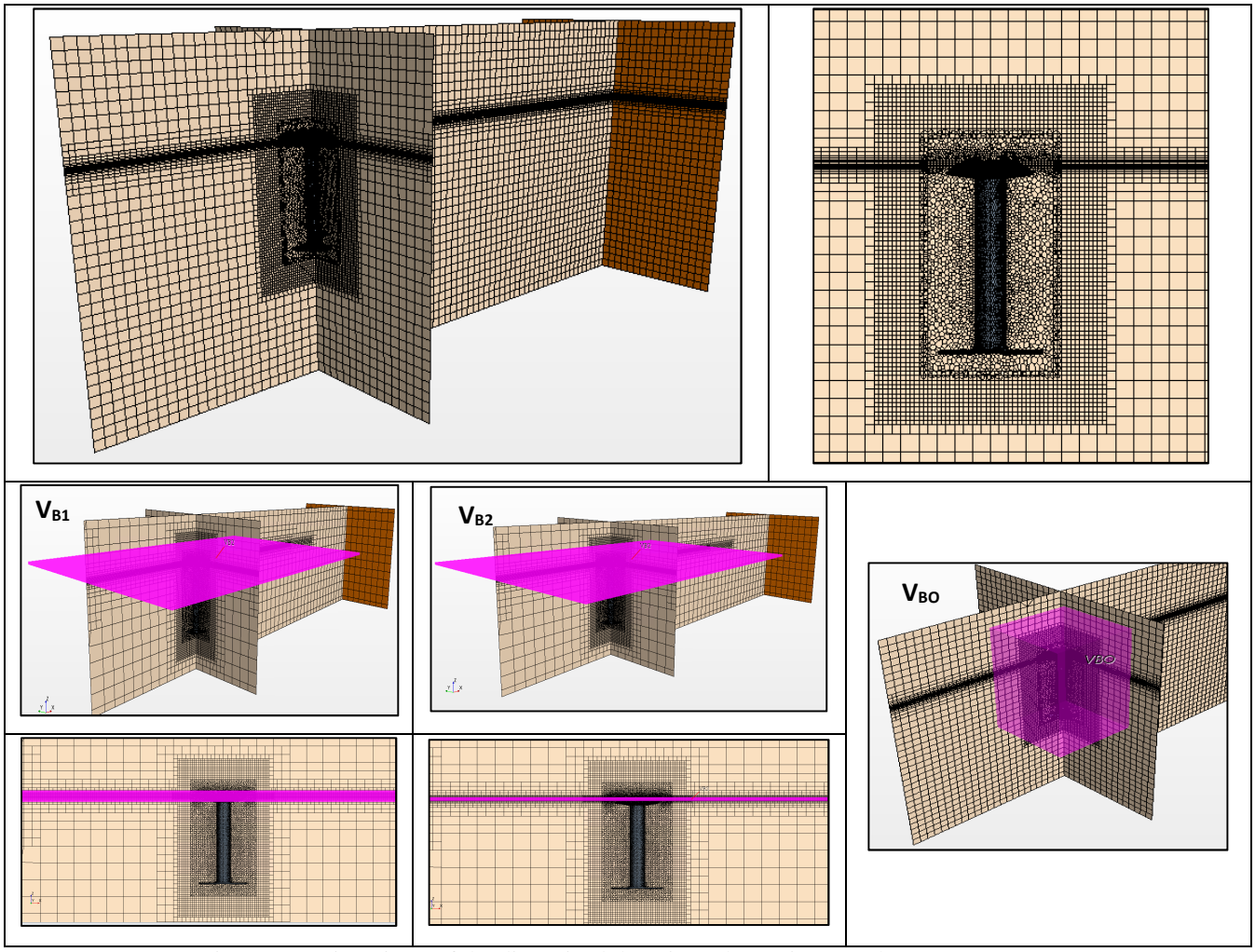


Figure 7 Section views of the discretized domain, volumetric controls ($V_{B1}$, $V_{B2}$,$V_{BO}$ )

The appropriate grid resolution is set after series of tests; 9 grids with different $V_{BO}$ dimensions, horizontal and vertical discretization are analyzed by means of regular wave state, $H_i$= 0.0175 m, $T_i$= 0.7 s, $\lambda_i$ = 0.77 m depth=0.53 m. The characteristics of each tested grid are summarized in **Errore. L'origine riferimento non è stata trovata.**. Through the normalized heave response, calculated as the ratio between the amplitude of the first harmonic of the heave response and the first harmonic of the wave elevation, [38], the effects of grid resolution and the domain dimensions on the dynamic response of the device are studied. The grid resolution around the overset region, generated through $V_{BO}$, does not strongly affect the heave response. It is observed that the convergence is guaranteed if the distance between the overset region boundaries and $V_{BO}$'s ones is kept larger than four cell layers. The largest variation induced by this parameter on the heave response was 2.6% of that calculated by means of the selected $V_{BO}$'s volume. Figure 8.a shows the results of this analysis, where the red point represents the adopted $V_{BO}$'s volume.

Table 1 Grid characteristics, in bold is the selected grid

| Grid n° | n° cells | Sidewall *[mm]* | $V_{B1}$ | | $V_{B2}$ | | $V_{BO}$ | | | RAO *[Heave/$H_i$]* |
|---|---|---|---|---|---|---|---|---|---|---|
| | | | $\Delta x=\Delta y$ *[mm]* | $\Delta z$ *[mm]* | $\Delta x=\Delta y$ *[mm]* | $\Delta z$ *[mm]* | $\Delta x=\Delta y=\Delta z$ *[mm]* | height *[mm]* | *side [mm]* | |
| 1 | 1.21E+06 | 250 | 16.0 | 8.0 | 12.8 | 1.7 | 8.0 | 562 | 188 | 0.296 |
| **2** | **1.14E+06** | **250** | **16.0** | **8.0** | **12.8** | **1.7** | **8.0** | **500** | **157** | **0.303** |
| 3 | 1.12E+06 | 250 | 16.0 | 8.0 | 12.8 | 1.7 | 8.0 | 500 | 141 | 0.311 |
| 4 | 7.04E+05 | 250 | 16.0 | 8.0 | 15.3 | 1.7 | 8.0 | 500 | 157 | 0.287 |
| 5 | 3.12E+06 | 250 | 16.0 | 8.0 | 6.3 | 1.7 | 8.0 | 500 | 157 | 0.310 |
| 8 | 9.20E+06 | 250 | 16.0 | 8.0 | 12.8 | 0.6 | 8.0 | 500 | 157 | 0.310 |
| 7 | 2.83E+06 | 250 | 16.0 | 8.0 | 12.8 | 1.3 | 8.0 | 500 | 157 | 0.307 |
| 8 | 1.18E+06 | 250 | 16.0 | 8.0 | 12.8 | 2.5 | 8.0 | 500 | 157 | 0.296 |
| 9 | 1.08E+06 | 250 | 16.0 | 8.0 | 12.8 | 3.1 | 8.0 | 500 | 157 | 0.284 |

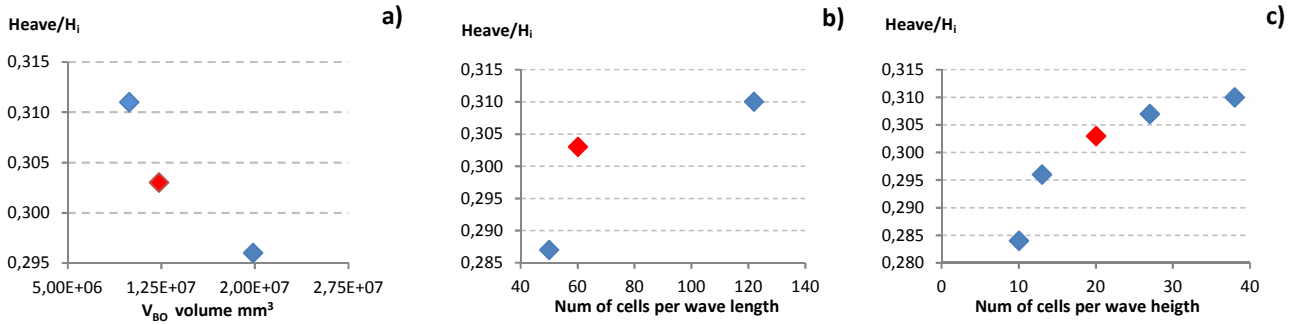


Figure 8 Results of the grid sensitivity analysis, a) $V_{BO}$'s dimensions effects, b) number of cells per wave length effects and c) number of cells per wave height effects

The grid resolution along the free surface, generated through $V_{B1}$ and $V_{B2}$ shows the largest effect on the heave response (around 6.7 % of that calculated with the final resolution) as well as on the required computational time. For these parameters, a compromise has to be taken between the required time and accuracy. Final choice for $V_{B2}$ horizontal discretization $\Delta x=\Delta y=\lambda_i/70$ while for vertical direction is $\Delta z=H_i/20$. Figure 8.b and Figure 8.c show the effects of this discretization, the red points represent the selected grid dimensions and related device heave response. The selected mesh characteristics contribute to generate a grid of variable cell numbers from $1.14\cdot10^6$ to $3.1\cdot10^6$ according with the incident wave condition. Grid 2 in **Errore. L'origine riferimento non è stata trovata.**is selected to carry out all the simulations, the final domain and grid setup are summarized in Figure 9. To assure the numerical stability and with respect to the requested Courant number, a time step equal to $T_i/400$ is adopted in the study. All the RANS simulations are carried out on the server at the hydraulic laboratory of the University of Bologna, each compute node consists of hexa-core 2.00 GHz Intel Xeon E5. For a mesh with 1.14 million elements, it takes about 220 h on 12 cores to complete 10 wave periods of time (4000 time steps).

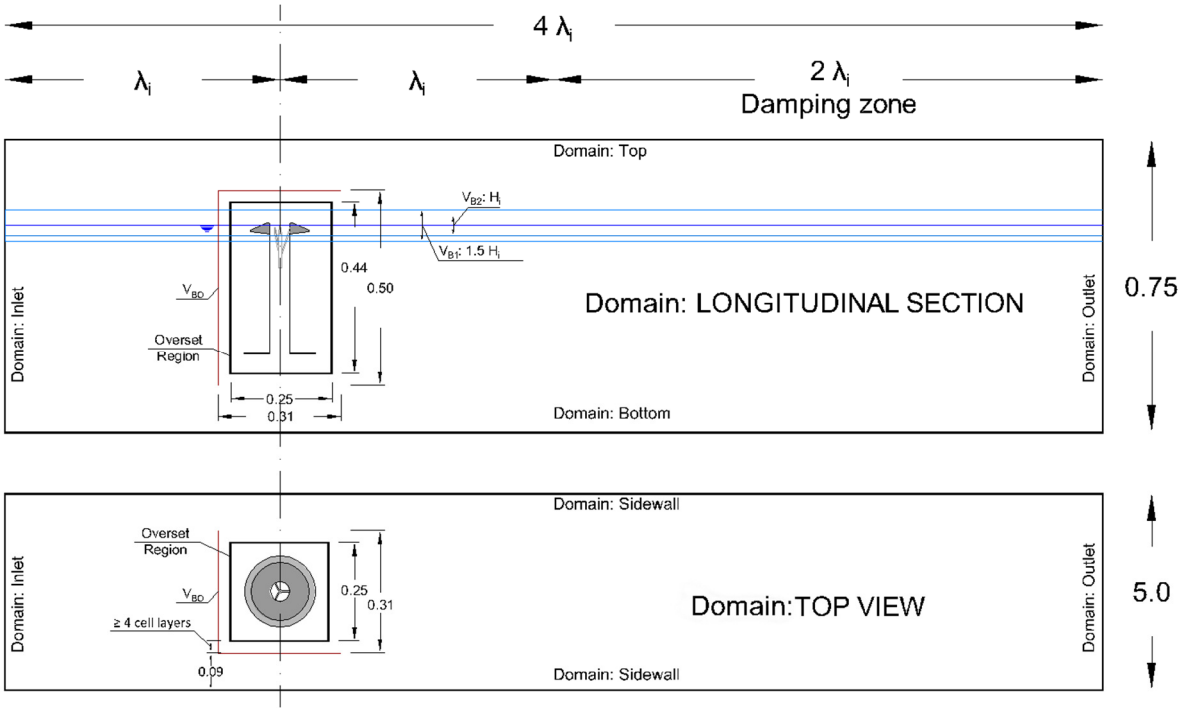


Figure 9 Final domain and grid setup

*5.3 Validation of the code through heave decay tests*

The experimental tests are performed at the Hydraulic laboratory of the University of Bologna. The main aim was to identify the hydrodynamic characteristics of the OXYFLUX device through a heave decay test, [10,39]. In this work those results have been used to validate the CFD model. Total mass of the 1/16 Froude scaled OXYFLUX model, including weight of the DOP transducer and its support structure, was 323 g for both experimental and numerical test. The numerical decay test was performed in a squared section computational domain with side equal to 2.0 m ( $-1.00 \le x;y \le 1.00$) and height equal to 0.75 m ( $-0.53 \le z \le 0.22$ ). The total number of elements used in the RANS simulation was around 1.45 million, with a resolution similar to grid 2. A damping layer zone of 0.50 m was adopted in front of all the far field boundaries to absorb radiated waves from the device. To perform the heave decay test, the OXYFLUX has been lifted with an initial displacement of +0.03 m. The upper panel in Figure 10 shows the comparison between normalized heave decay results obtained from numerical simulation and the experimental measurements. Numerical results agree with experimental data; the natural heave decay period was 1.08 s while 1.04 s is detected for the physical calm water test confirming the capacity of the numerical model to capture the dynamic of the OXYFLUX. To perform the numerical pith decay test, the OXYFLUX model was rotated around its center of mass with an initial angle of 3 degrees. The observed pitch natural period was 1.85 s (see Figure 10 lower panel). Concluding, the grid-sensitivity analysis, which has been presented in the previous section, and the validation decay test study as well as the comparison between heave displacement plotted in Figure 11, indicate that the mesh and the adopted numerical settings are reliable for further analysis on the OXYFLUX device.

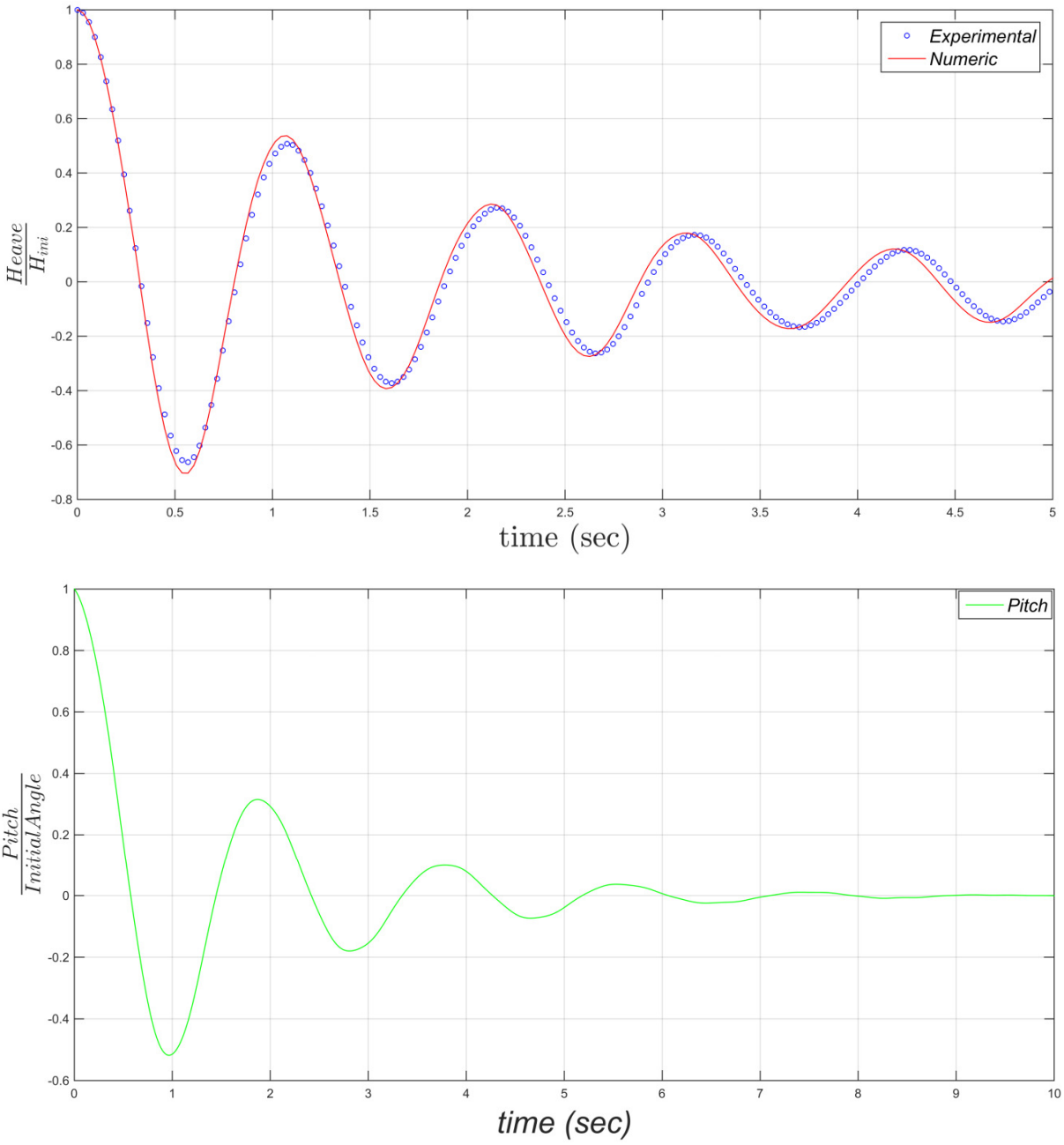


Figure 10 Comparison between numerical and physical heave decay test results (upper panel), numerical results for pitch decay test (lower panel)

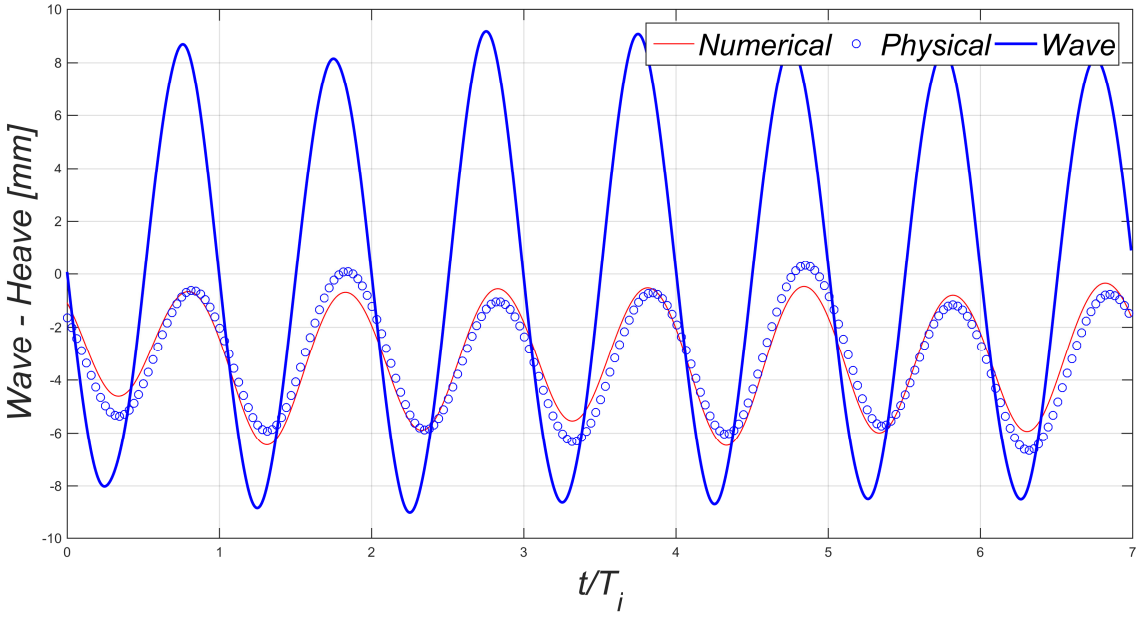


Figure 11 Comparison of experimental and numerical time history of heave displacement, Hi=0.018 m Ti=0.70 s

## 7. Results and discussion

### *6.1 Analysis of the induced wave height effects*

A series of simulations are performed to investigate nonlinear effects due to the interaction between waves and the OXYFLUX model. Six numerical simulations are completed to reach this scope. Each simulation is characterized by regular waves with different heights and constant periods. In order to reduce the required simulation time, the shortest wave period is used, (i.e. 0.70 s), while the wave heights range is between 0.013 m and 0.042 m. For each test, heave response and phase shift between device and water surface are examined. The numerical RAO (Response Amplitude Operator) is evaluated by means of time domain analysis, (zero up-crossing procedure), thus the final results is the average value of the ratio between the amplitudes of the heave mode and the corresponding incident wave amplitudes. Figure 12 shows the resulting RAO on the incident wave heights highlighted through different colors in order to uniquely define the response. Heave amplitude increases up to wave height equal to 0.023 m. Whereas, if the wave height increases driving up relative velocity between water and device, viscous dissipation becomes more important reducing the amplitude and increasing phase shift up to 0.06 s. The increase of the phase shift indicates that the system is subjected to a larger damping for larger waves. As it was expected, nonlinear effects introduce additional damping forces that reduce the heave amplitude and generate a phase shift, causing the required degree of overtopping. This also occurs for small and short waves that are caused by the breeze.

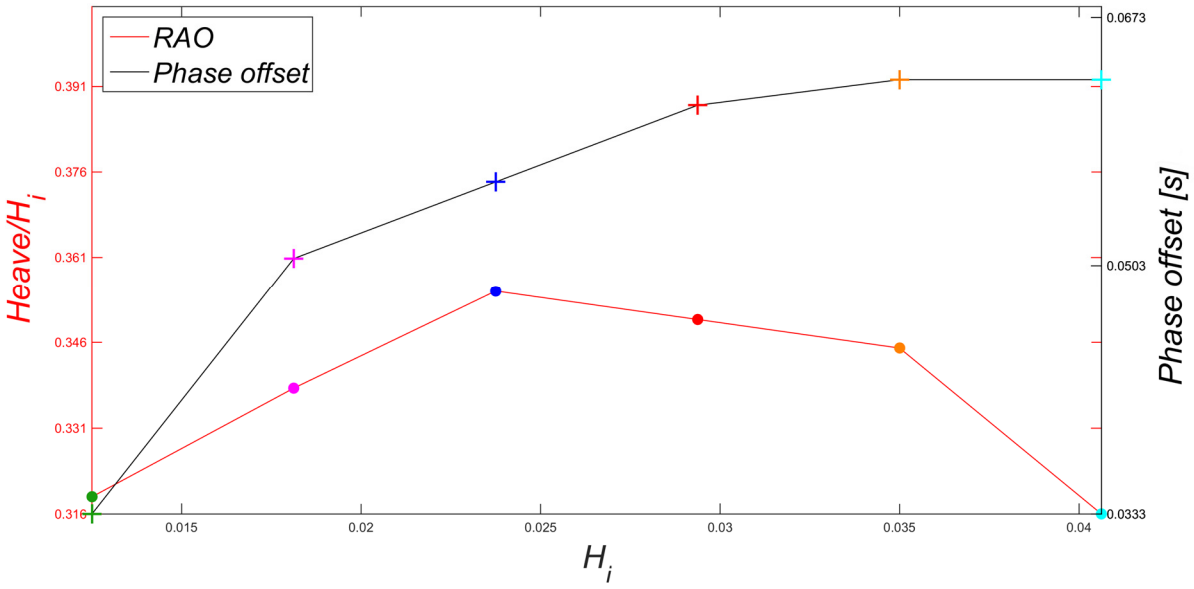


Figure 12 Heave response (red line) and phase shift (black line), Ti=0.70 s.

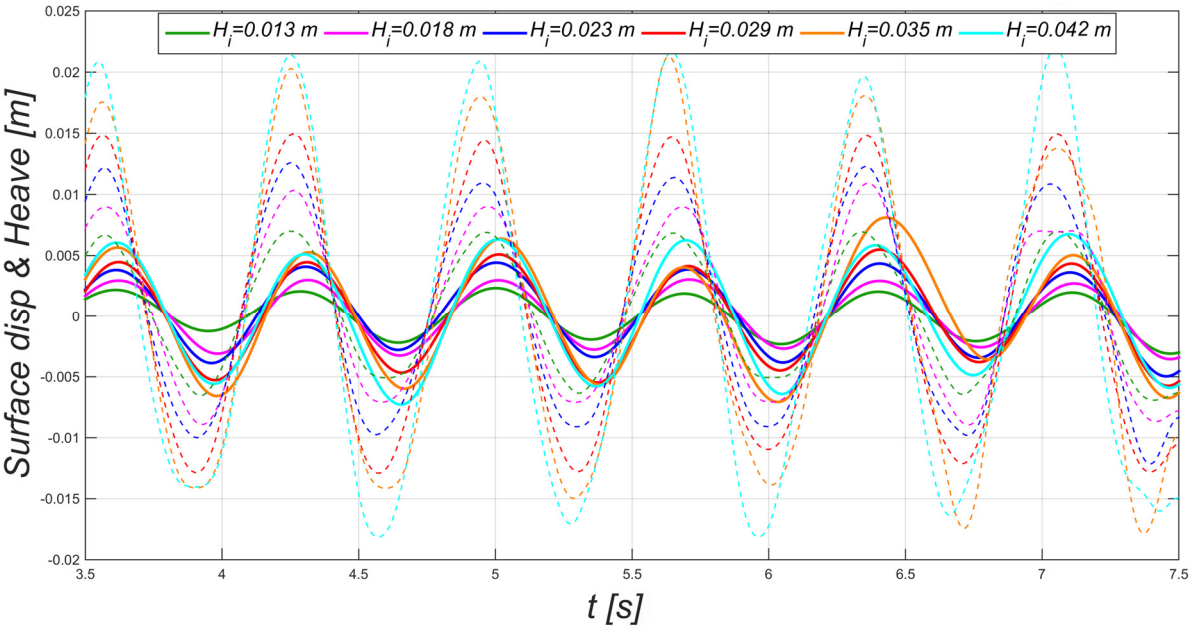


Figure 13 Recorded time series, dotted lines represent the water surface while solid lines the heave motion,

*6.2 OXYFLUX performance in regular wave*

This section addresses the performance of the OXYFLUX in regular waves in terms of heave and pitch response and pumped water. Effects of different regular waves on the hydrodynamic response and pumping performance are investigated through 13 wave conditions (see Table 2) with heights ranging between 0.018 m and 0.056 m and periods ranging between 0.70 and 1.30 s .

Table 2: Simulated wave states

| $H_i$ [m] | 0.018 | 0.023 | 0.026 | 0.029 | 0.031 | 0.034 | 0.039 | 0.042 | 0.044 | 0.045 | 0.048 | 0.050 | 0.056 |
|---|---|---|---|---|---|---|---|---|---|---|---|---|---|
| $T_i$ [s ] | 0.70 | 0.75 | 0.8 | 0.85 | 0.90 | 0.95 | 1.00 | 1.05 | 1.10 | 1.15 | 1.20 | 1.25 | 1.30 |
| $s[H_i/L_i\,\%]$ | 2.36 | 2.64 | 2.63 | 2.63 | 2.53 | 2.53 | 2.66 | 2.65 | 2.59 | 2.47 | 2.48 | 2.44 | 2.58 |

In the following section only time series from the first wave state presented in Table 2 is discussed in detail. Whereas, results coming from the other wave states will be later summarized in Figure 17 and Figure 19. Figure 14 shows time series and frequency analysis of the instantaneous pumped water, heave and pitch response and incident wave for 0.018 m wave height and 0.70 s wave period. In this case, the incident period is shorter than the heave resonant period. The heave response does not follow the motion of the water surface and is smaller than the incident wave height, RAO value is 0.303. Phase shift between water surface and floating-body is not pronounced, because the wave height is too small to strongly affect the dynamic behavior via non-linear effects, inducing more important phase shifting. Moreover, motion of the fluid particles, as well as excitation force due to the incident wave, decrease rapidly with the increasing depth below the free surface, which near the bottom are almost null. Therefore, the force acting on the floater is larger than that applied at the stabilizing ring, which moves in calm water driven by the floater's motion. In these conditions, viscous drag is the result of flow separation and vortex shedding at ring corner, and becomes the dominant damping source for the device. Such a behavior was searched as a main mode of operation during the designing phase with the aim to generate wave overtopping, even during the smallest summer's wave states (see Figure 14 and Figure 15).

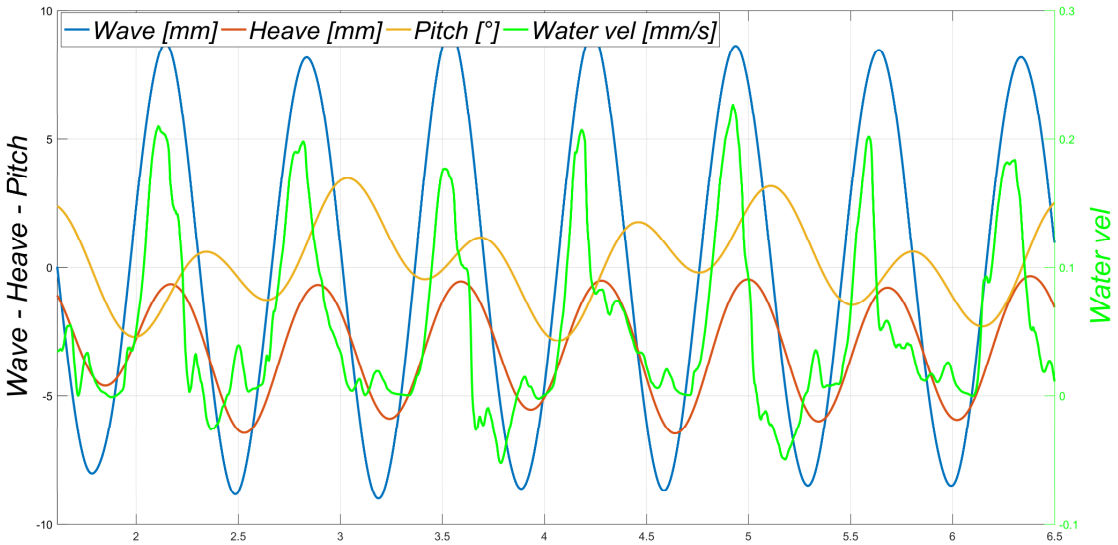

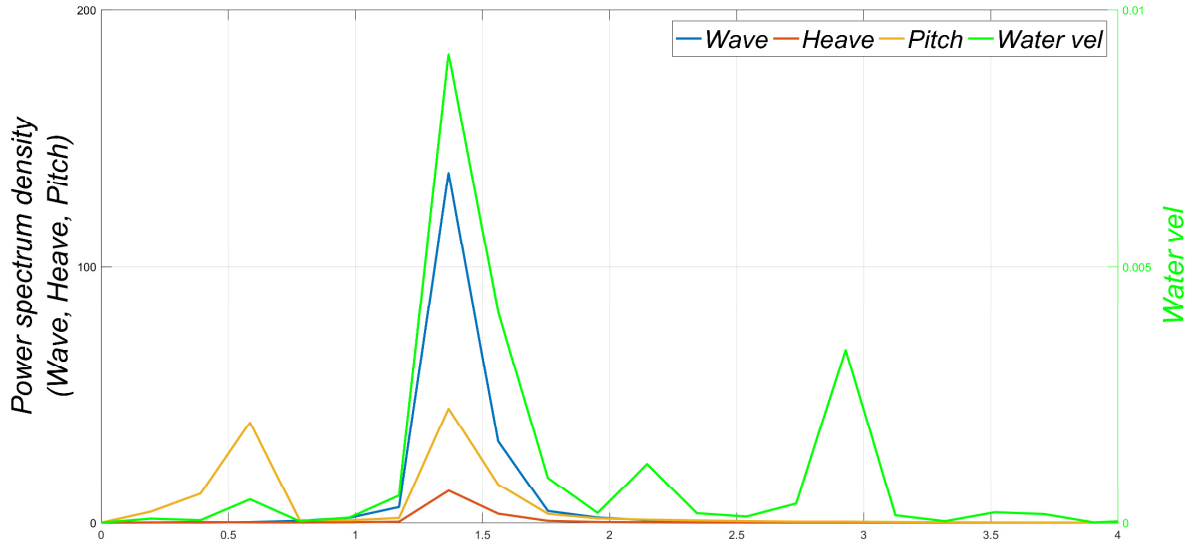


418 Figure 14 Heave, pitch and pumping performance response, $H_i$=0.018 m $T_i$=0.70 s , (black line is referred to the
419 freeboard crest of the device). Recorded time series (upper panel), time series frequency analysis (lower panel).
420

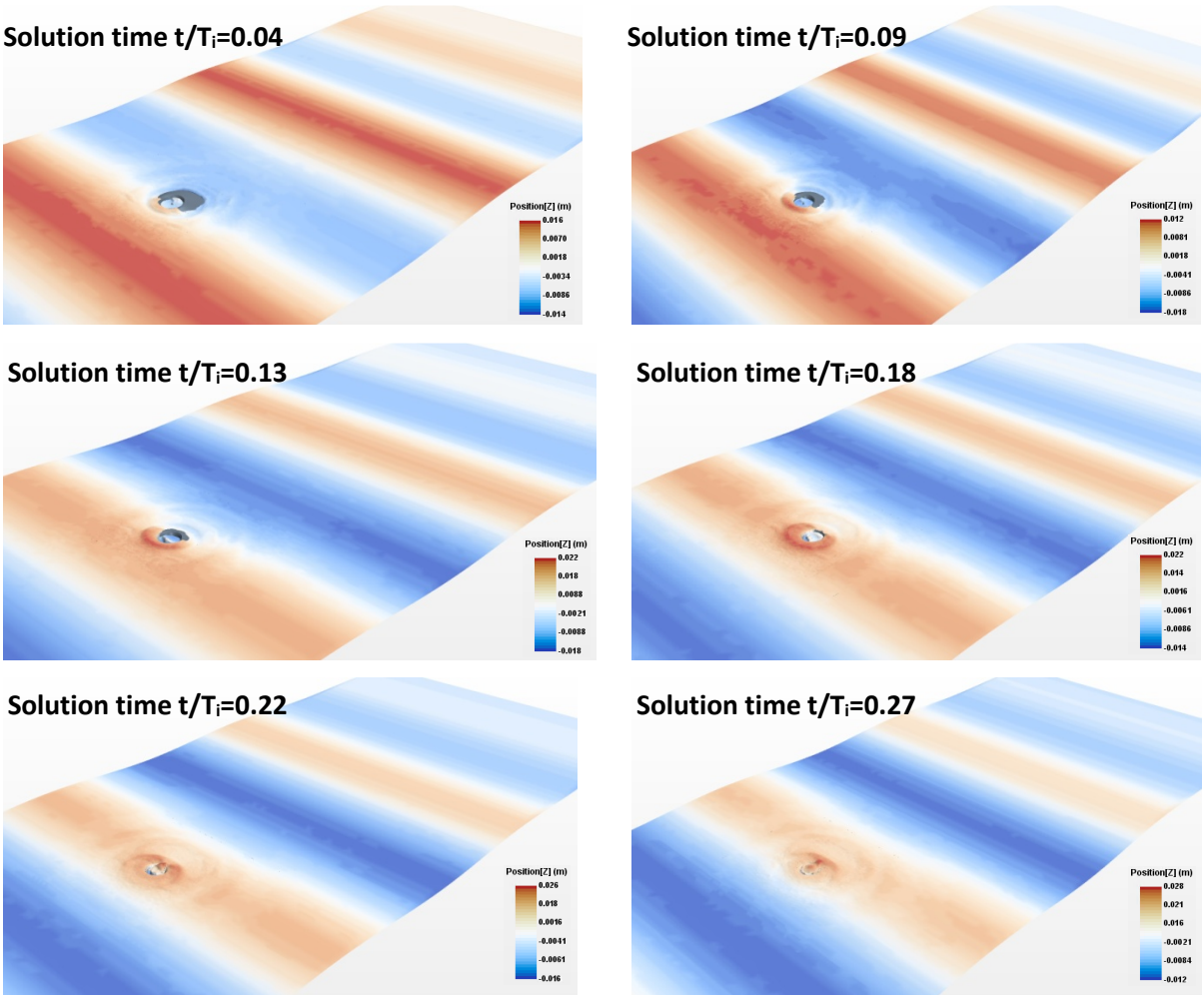

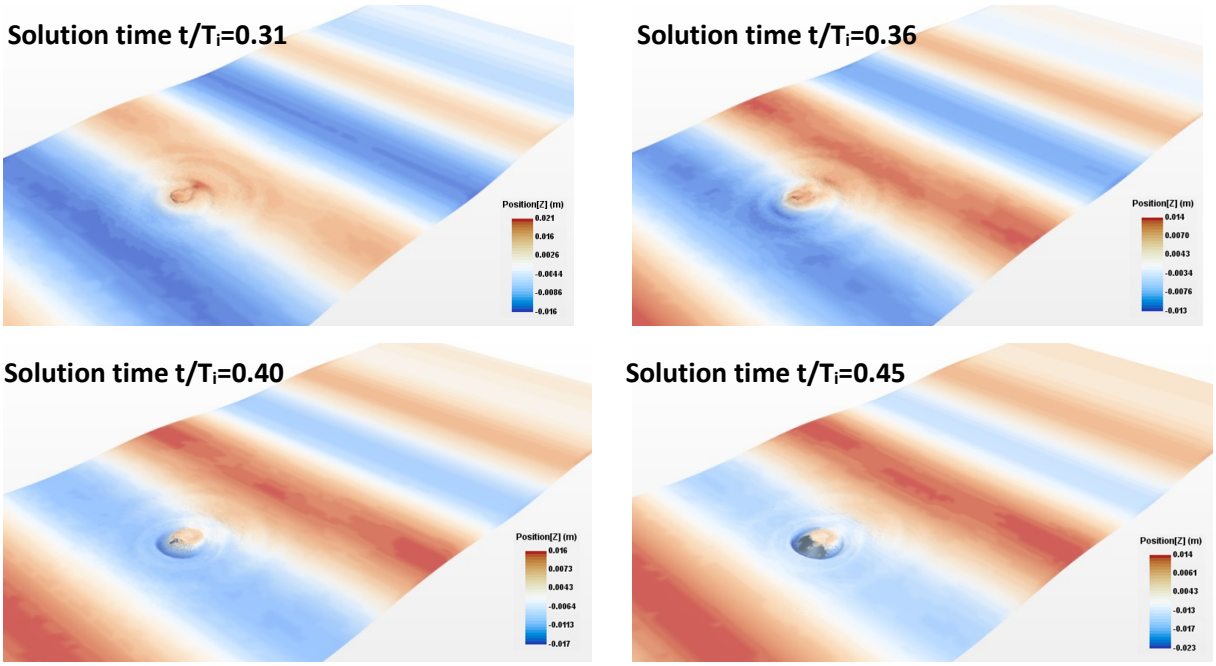


Figure 15: Images sequence of wave device interaction. Smallest wave state, ($H_i$=0.018 m $T_i$=0.70 s).

Pitch response exhibits two peaks (yellow line Figure 14 lower panel): the first one, around 1.42 Hz corresponds to the incident wave frequency. The second one occurs at frequencies around 0.54 Hz (natural pitch frequency). This is probably caused by a nonlinear effect, resulting from the coupled effect between heave and pitch modes, usually called Mathieu-type instability, [40,41]. This instability is caused by the dynamic variation in the device's metacentric height (consequence of the heave motion), which changes during the wave cycle and consequently makes the device unstable, causing the high amplitudes in the pitch modes. This effect has been reported by other authors for similar floating structures [40,42–45] and is responsible for the nonlinearities observed in Figure 14 at frequencies around 0.54 Hz. The same non-linear response is observed for the other simulated wave states. Pitch mode is also of interest for the pumping performance, since it affects the capacity of the floater mouth to catch the water from the wave crest. It becomes more important during the back side overtopping, which happen a second time during the wave attack, as discussed below. The pumped water is driven by the overtopping phenomenon and by the heave mode, which lead to a main cyclic flux with a characteristic period comparable to the incident wave. Lower panel in Figure 14 shows the spectral density of the wave, heave and flow rate. Flow rate exhibits a second less intense peak, occurring at 2.90 Hz (double of the wave frequency). This is mainly due by the combined action of the pitch mode and wave action on the back side of the floater. At the beginning of the wave attack, the crest overtops the device through its front side going up on the frontal region of the floater. Later, part of the wave crest that has not overtopped the catching mouth, flows around the circular shape of the floater combining one to each other on the back side producing a second overtopping contribution. Figure 16 highlights how this process occurs in the physical modelling, (upper panel) and how the numerical

model reproduces it, (bottom panel). Despite such an overtopping, functioning is always present for all the simulated wave states. The intensity of the second flow rate peak as well as the amplitude of the non-linear pitch oscillations increase reaching the heave resonant frequency.

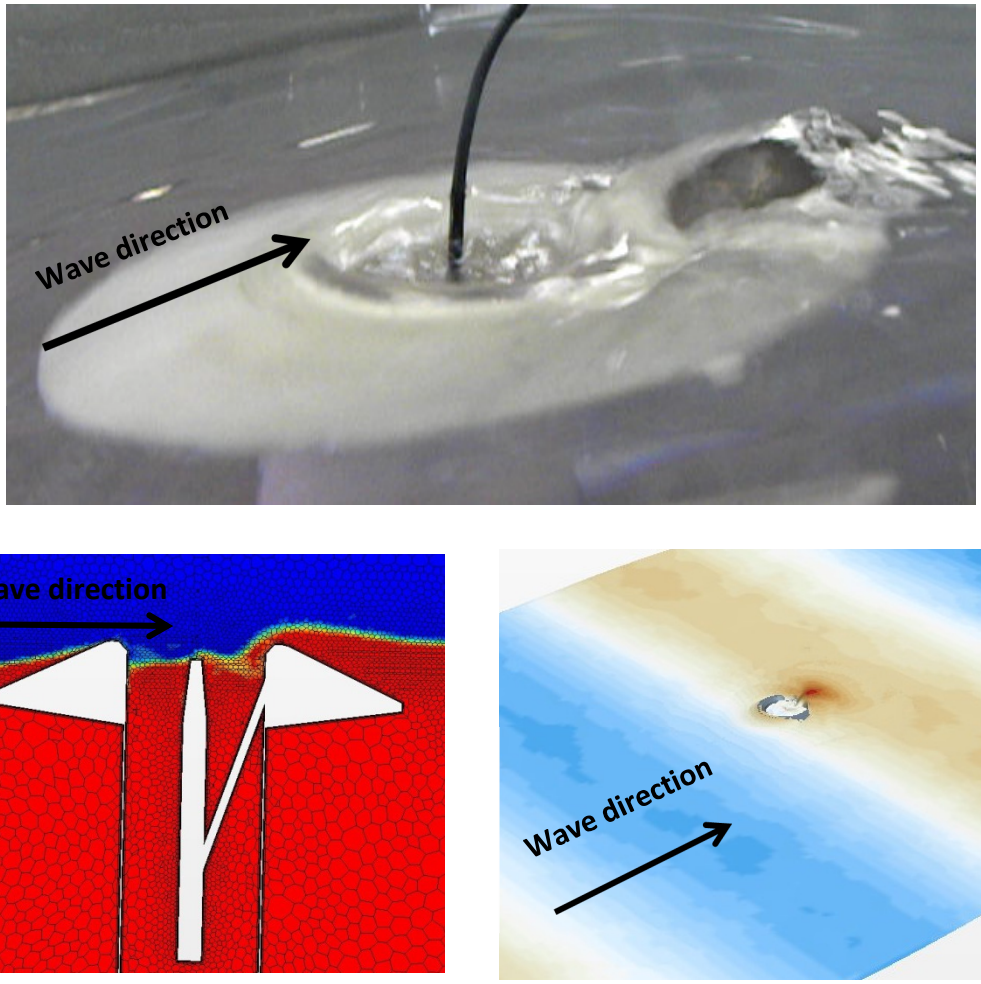


Figure 16: Second overtopping contribution which happen in the back side of the OXYFLUX, comparison between physical (upper panel) and numerical (upper panel)

Comparison between numerical and experimental heave RAO is shown in Figure 17, where generalized slight differences exist between the experimental and numerical results. The experimental data shows a lower heave response when compared with the numerical prediction for the entire range of tested wave periods. However, experimental and numerical results tend to converge once the incident wave period is far from the heave resonant period. This suggests important dissipations of energy, due to the mooring lines used in physical modelling and not modelled in the RANS simulations. The larger heave displacements close to the resonant period, generate important viscous dissipations due to the interaction of the cables and the surrounding water. Moreover, values of RAO lower than 1, for periods higher than the natural one, are observed. Such a behavior is attributed to non-linear effects which grow with the increase of the wave heights, that in this study grow, according to the wave periods as shown in Table 2. Despite no physical

data being available for the pitch mode, RAOs are calculated from the numerical simulations and the results are depicted in Figure 18. Pitch rigid rotation shows an increasing trend according to simulated wave heights and growth periods. But no resonant period is reached for the tested sea states, as proved by the absence of a clear response peak. Results for wave period between 1.1 s and 1.2 s show the larger increment for pitch rotations, suggesting a transfer of energy between the heave and pitch modes at incident wave periods. This is close to the resonant frequency of the OXYFLUX heaving mode. The presence of the mooring arrangement, which would change the center of rotation of the device and would lower the sensibility of pitch mode to the varying of the device's metacentric height, would reduce this energy transfer.

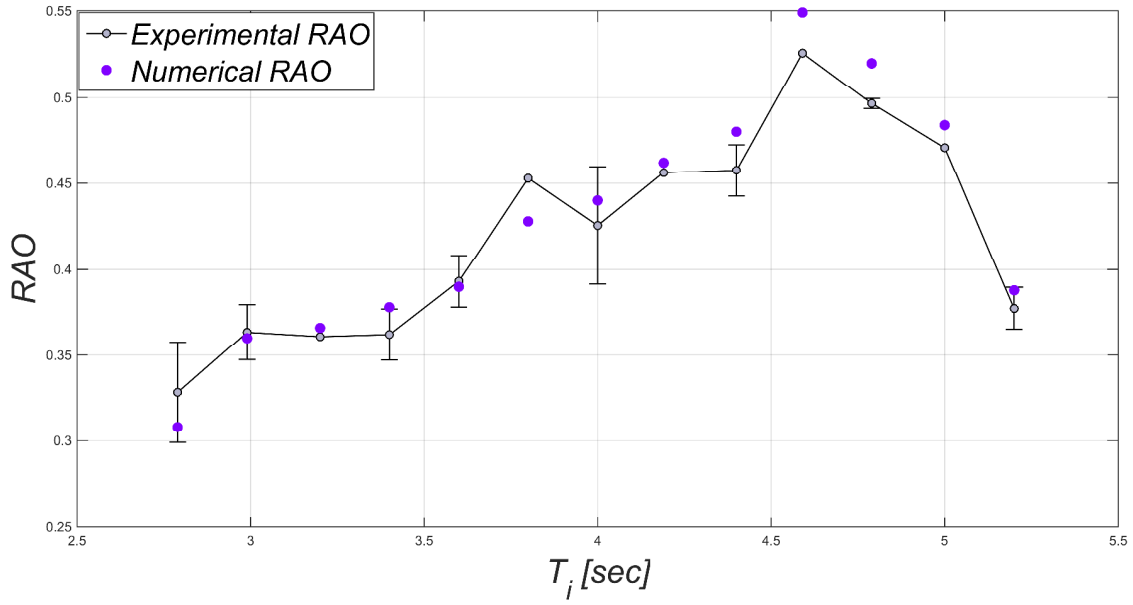


Figure 17: Experimental and numerical heave RAO. Red dots are the RAO values related to the wave states in Table 2

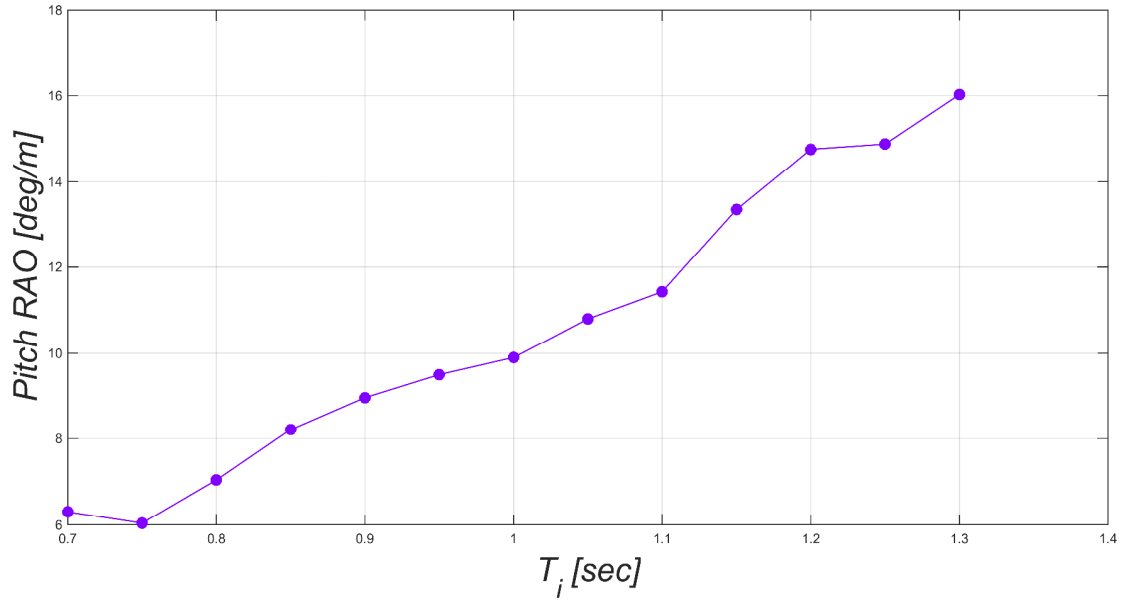


Figure 18: Numerical pitch RAO.

For each simulated wave state, instantaneous average value of the flow is measured through an artificial interface applied on the floater mouth, see Figure 6. The resulting time series allows calculating the integral averaged value of the flow rate and the average water velocity over five wave cycles. Figure 19 shows the comparison of numerical and physical water velocity values, non-dimensionalised with $\sqrt{g \cdot H_i}$ as a function of $H_i/R_c$, according to [10] where $R_c$ denotes the OXYFLUX freeboard. Overall, good general agreement for both the velocity values and the wave heights, at which these values occur, is reached. The same specific trend of the water velocities values can be recognized according to the values of $H_i/R_c$. For low $H_i/R_c$ ratio, only part of the wave crest is captured by the floater mouth and used to generate the required head to pump the water downward. High values of $H_i/R_c$ ratio correspond to the longest and highest waves for which the height of the device freeboard assumes not great importance. The wave crest flows over the floater but does not go into it. That makes possible an inversion of the flux direction mainly due to the depression induced at the floater mouth by the water, which runs over the device and draws the water inside the pipe. The comparison between the experimental and numerical results presented in Figure 19, shows that the numerical model is able to reproduce the described complex OXYFLUX's pumping mechanism.

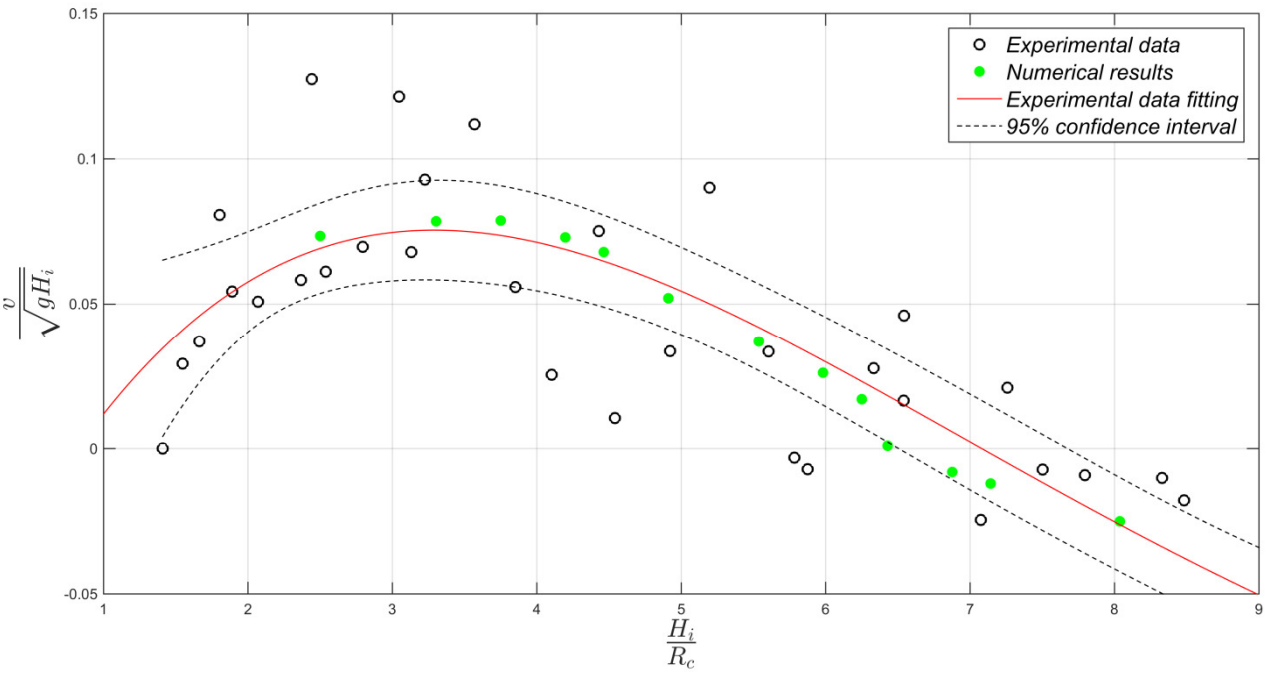


Figure 19: Comparison between experimental and numerical dimensionless water velocity, $R_c$ denotes the device freeboard

## 8. Conclusion

The RANS solver Star-CCM+, is adopted to analyse an innovative wave pump device called OXYFLUX. The first aim of the presented paper was to reproduce the experimental condition and results obtained during the physical modelling carried out at the University of Bologna. The same OXYFLUX 1/16 Froude scale geometry as well as a numerical domain width equal to the physical flume is used to reach this scope through all the CFD simulations. The dynamic overset approach is adopted to investigate heave and pitch decay tests as well as the OXYFLUX dynamic response under 13 regular wave. The adopted grid and numerical settings were selected after a sensitivity study, while the model is validated by means of comparison between the physical and numerical heave decay tests and the comparison of the heave displacement time series. Good agreement is also observed within comparison of heave RAO and dimensionless pumped water velocity. Thus, regarding the proposed numerical model, it can be concluded that the adopted overset mesh and numerical settings are reliable for future analysis on the OXYFLUX. Hence, the simulations carried out by the validated model provide some useful results. Second aim of the paper was to investigate the non-linear effects of due to the wave heights on the OXYFLUX dynamic response. Such a purpose has been achieved by means of 6 regular waves characterized by constant periods and different heights.

The OXYFLUX pumping capacity increases thanks to the viscous dissipations, that affect the heave response in terms of magnitude and phase shift. The additional nonlinear forces caused by flow separation and vortex shedding at the stabilizing ring corners, not only become more significant when the wave heights are large, but can also affect the pumping performance in smaller wave conditions typical of the summer waves due to the breeze; i.e. conditions that are typical of the anoxic events. Furthermore, by means of the measurement section at the top of the floater, is has been observed that the instantaneous pumping rate is characterised by two peaks in the same wave cycle. The first one is due to the initial overtopping action and mainly occurs in the frontal area of the floater, while the second one occurs on the back region of the floater. It is less intense and is due to the action of the wave crests around the catching circular mouth combined with the pitch motion. Pitch mode response shows two principal harmonics for all the simulated wave states. The largest harmonic always appears at the wave frequency. The second harmonic appears around the pitch natural frequency of 0.54 Hz as a consequence of Mathieu’s instability and is generally smaller than the first one. A second proof of the coupling between the heave and pitch modes is also suggested by the larger increment of the pitch RAO values for wave periods between 1.1 s and 1.2 s, whom correspond the resonant period of the OXYFLUX's heave mode. This phenomenon might be reduced by the presence of mooring system which would change the center of rotation and would lower the sensibility of the pitch mode to the varying of the device metacentric height. The combined heave and pitch motion should be more deeply investigated in order to avoid the fully extension of a possible mooring chain

system. Further development and studies should involve an improvement of the time domain numerical model which should be extended to include surge mode and mooring system and the improvement of the floater shape.

The developers and authors believe that a fully optimized device might be used as an effective tool to counteract the anoxia at the bottom layers near mussel farm in areas like the Northern Adriatic or Baltic Sea.

## 9. References


[1] Howarth RW, Billen G, Swaney D, Townsend A, Jaworski N, Lajtha K, et al. Regional nitrogen budgets and riverine N & P fluxes for the drainages to the North Atlantic Ocean: Natural and human influences. Biogeochemistry 1996;35:75–139. doi:10.1007/BF02179825.

[2] Diaz RJ. Overview of hypoxia around the world. J Environ Qual 2001;30:275–81. doi:10.2134/jeq2001.302275x.

[3] Caddy JF. Toward a comparative evaluation of human impacts on fishery ecosystems of enclosed and semi-enclosed seas. Rev Fish Sci 1993;1:57–95. doi:10.1080/10641269309388535.

[4] Isaacs JD, Castel D, Wick GL. Utilization of the energy in ocean waves. Ocean Eng 1976;3:175–87. doi:10.1016/0029-8018(76)90022-6.

[5] Kenyon KE. Upwelling by a wave pump. J Oceanogr 2007;63:327–31. doi:10.1007/s10872-007-0031-8.

[6] Liu CCK, Jin Q. Artificial upwelling in regular and random waves. Ocean Eng 1995;22:337–50. doi:10.1016/0029-8018(94)00019-4.

[7] Maruyama S, Tsubaki K, Taira K, Sakai S. Artificial upwelling of deep seawater using the perpetual salt fountain for cultivation of ocean desert. J Oceanogr 2004;60:563–8. doi:10.1023/B:JOCE.0000038349.56399.09.

[8] Stommel H, Arons AB, Blanchard D. An oceanographic curiosity: the perpetual salt fountain. Deep Res 1956;3:152–3.

[9] Nam BW, Shin SH, Hong KY, Hong SW. Numerical Simulation of Wave Flow over the Spiral-Reef Overtopping Device. Proc. Eighth ISOPE Pacific/Asia Offshore Mech. Symp., 2008, p. 262–7.

[10] Antonini A, Lamberti A, Archetti R. Oxyflux, an innovative wave driven device for the oxygenation of deep layers in coastal areas: a physical investigation. Coast Eng 2015, 104, 54-68. DOI: 10.1016/j.coastaleng.2015.07.005

[11] Margheritini L, Claeson L. An Innovative Way of Utilizing Wave Energy to Counteract Eutrophication and Hypoxia. Proceeding 9th Eur. Wave Tidal Energy Conf., Southampton: 2011.

[12] Vantorre M, Banasiak R, Verhoeven R. Modelling of hydraulic performance and wave energy extraction by a point absorber in heave. Appl Ocean Res 2004;26:61–72. doi:10.1016/j.apor.2004.08.002.

[13] Folley M, Whittaker T. Spectral modelling of wave energy converters. Coast Eng 2010;57:892–7. doi:10.1016/j.coastaleng.2010.05.007.

[14] Bozzi S, Miquel AM, Antonini A, Passoni G, Archetti R. Modeling of a point absorber for energy conversion in Italian seas. Energies 2013;6:3033–51. doi:10.3390/en6063033.

566 [15] Korde U a. Efficient primary energy conversion in irregular waves. Ocean Eng 1999;26:625–51.
567 doi:10.1016/S0029-8018(98)00017-1.

568 [16] Bjarte-Larsson T, Falnes J. Laboratory experiment on heaving body with hydraulic power take-off
569 and latching control. Ocean Eng 2006;33:847–77. doi:10.1016/j.oceaneng.2005.07.007.

570 [17] Kofoed JP, Frigaard P, Friis-Madsen E, Sørensen HC. Prototype testing of the wave energy converter
571 wave dragon. Renew Energy 2006;31:181–9. doi:10.1016/j.renene.2005.09.005.

572 [18] Yu Y-H, Li Y. A RANS Simulation of the Heave Response of a Two-Body Floating Point Wave Absorber.
573 Proc 21st Int Offshore Polar Eng Conf 2011:1–10.

574 [19] Agamloh EB, Wallace AK, von Jouanne A. Application of fluid-structure interaction simulation of an
575 ocean wave energy extraction device. Renew Energy 2008;33:748–57.
576 doi:10.1016/j.renene.2007.04.010.

577 [20] Bhinder M, Mingham C, Causon D. Numerical and experimental study of a surging point absorber
578 wave energy converter. Proceeding 28th Int. Conf. Ocean. offshore Arct. Eng., Honolulu: 2009.

579 [21] Yu YH, Li Y. Reynolds-Averaged Navier-Stokes simulation of the heave performance of a two-body
580 floating-point absorber wave energy system. Comput Fluids 2013;73:104–14.
581 doi:10.1016/j.compfluid.2012.10.007.

582 [22] Chan WM. Overset grid technology development at NASA Ames Research Center. Comput Fluids
583 2009;38:496–503. doi:10.1016/j.compfluid.2008.06.009.

584 [23] Artegiani a., Paschini E, Russo a., Bregant D, Raicich F, Pinardi N. The Adriatic Sea General
585 Circulation. Part I: Air–Sea Interactions and Water Mass Structure. J Phys Oceanogr 1997;27:1492–
586 514. doi:10.1175/1520-0485(1997)027<1492:TASGCP>2.0.CO;2.

587 [24] Masina M, Lamberti A, Archetti R. Coastal flooding: A copula based approach for estimating the joint
588 probability of water levels and waves. Coast Eng 2015;97:37–52.
589 doi:10.1016/j.coastaleng.2014.12.010.

590 [25] Schweizer J, Antonini A, Govoni L, Gottardi G, Archetti R, Supino E, et al. Investigating the potential
591 and feasibility of an offshore wind farm in the Northern Adriatic Sea. Appl Energy 2016;177.
592 doi:10.1016/j.apenergy.2016.05.114.

593 [26] CD-ADAPCO. Star-CCM+ 8.04 User Manual. 2013.

594 [27] Menter FR. Two Equation Eddy Viscosity Turbulence Models For Engineering Applications. Aiaa
595 1994;32:1598–605.

596 [28] Hirt C., Nichols B. Volume of fluid (VOF) method for the dynamics of free boundaries. J Comput Phys
597 1981;39:201–25. doi:10.1016/0021-9991(81)90145-5.

598 [29] Muzaferija S, Perić M. Computation of free surface flows using interface-tracking and interface-
599 capturing methods. In: WIT Press, editor. Nonlinear Water Wave Interact., Southampton: 1999, p.
600 59–100.

601 [30] Tezdogan T, Demirel YK, Kellett P, Khorasanchi M, Incecik A, Turan O. Full-scale unsteady RANS CFD
602 simulations of ship behaviour and performance in head seas due to slow steaming. Ocean Eng
603 2015;97:186–206. doi:10.1016/j.oceaneng.2015.01.011.

604 [31] Antonini A. Wave driven devices for the oxygenation of bottom layers. University of Bologna, 2014.
605 doi:10.6092/unibo/amsdottorato/6620.

606 [32] Zhao X, Ye Z, Fu Y, Cao F. A CIP-based numerical simulation of freak wave impact on a floating body.
607 Ocean Eng 2014;87:50–63. doi:10.1016/j.oceaneng.2014.05.009.

608 [33] Muliawan MJ, Gao Z, Moan T, Babarit A. Analysis of a Two-Body Floating Wave Energy Converter

With Particular Focus on the Effects of Power Take-Off and Mooring Systems on Energy Capture. J Offshore Mech Arct Eng 2013;135:031902. doi:10.1115/1.4023796.

[34] Choi J, Yoon SB. Numerical simulations using momentum source wave-maker applied to RANS equation model. Coast Eng 2009;56:1043–60. doi:10.1016/j.coastaleng.2009.06.009.

[35] Santo H, Taylor PH, Bai W, Choo YS. Current blockage in a numerical wave tank: 3D simulations of regular waves and current through a porous tower. Comput Fluids 2015;115:256–69. doi:10.1016/j.compfluid.2015.04.005.

[36] Demirel YK, Khorasanchi M, Turan O, Incecik A, Schultz MP. A CFD model for the frictional resistance prediction of antifouling coatings. Ocean Eng 2014;89:21–31. doi:10.1016/j.oceaneng.2014.07.017.

[37] Schultz MP, Swain GW. The influence of biofilms on skin friction drag. Biofouling 2000;15:129–39. doi:10.1080/08927010009386304.

[38] Drummen I, Wu M, Moan T. Experimental and numerical study of containership responses in severe head seas. Mar Struct 2009;22:172–93. doi:10.1016/j.marstruc.2008.08.003.

[39] Antonini A, Gaeta MG, Lamberti A. Wave - Induced devices for the oxygenation of deep layer: A physical investigation. Proc 33rd Conf Coast Eng, 2012.

[40] Rho JB, Choi HS, Shin HS, Park IK. A study on Mathieu-type instability of conventional spar platform in regular waves. Int J Offshore Polar Eng 2005;15:104–8.

[41] Gomes RPF, Henriques JCC, Gato LMC, Falcão a FO. Testing of a small-scale floating OWC model in a wave flume. Int Conf Ocean Energy 2012:1–7.

[42] Koo BJ, Kim MH, Randall RE. Mathieu instability of a spar platform with mooring and risers. Ocean Eng 2004;31:2175–208. doi:10.1016/j.oceaneng.2004.04.005.

[43] Li B Bin, Ou JP, Teng B. Numerical investigation of damping effects on coupled heave and pitch motion ofan innovative deep draft multi-spar. J Mar Sci Technol 2011;19:231–44.

[44] Yang H, Xiao F, Xu P. Parametric instability prediction in a top-tensioned riser in irregular waves. Ocean Eng 2013;70:39–50. doi:10.1016/j.oceaneng.2013.05.002.

[45] Tarrant K, Meskell C. Investigation on parametrically excited motions of point absorbers in regular waves. Ocean Eng 2016;111:67–81. doi:10.1016/j.oceaneng.2015.10.041.